Nuclear Inst, and Methods in Physics Research B 428 (2018) 47–55

Contents lists available at ScienceDirect

Nuclear Inst. and Methods in Physics Research B

journal homepage: www.elsevier.com/locate/nimb

Design and performance study of four-layer radio-voltaic and dual-effect nuclear batteries based on γ-ray

Zhangang Jin[a], Xiaobin Tang[a,*], Xiao Guo[a], Yunpeng Liu[a], Zhiheng Xu[a], Wang Chen[a], Dayong Zhou[b]

[a] Department of Nuclear Science and Engineering, Nanjing University of Aeronautics and Astronautics, 29 General Road, Jiangning District, Nanjing 211106, China
[b] Shanghai Institute of Space Power Sources, Shanghai 200245, China

ARTICLE INFO

Keywords:
AlGaInP device
Fluorescent layer
Dual-effect nuclear battery
Four-layer structure

ABSTRACT

Two kinds of four-layer nuclear batteries based on γ-ray, AlGaInP semiconductor PN junction, and ZnS:Cu fluorescent materials were prepared. One was a four-layer radio-voltaic nuclear battery (FRVB) with a volume of 1.00 cm^3, and another is a four-layer dual-effect nuclear battery (FDEB) with a volume of 1.03 cm^3. The output performance levels of the two batteries were tested with the irradiation of an X-ray tube. Results show that the output power of the nuclear battery in parallel is significantly greater than that in the series. However, the output power and power density of FDEB in parallel, which were 57.26 nW and 55.59 nW/cm^3, respectively, both five times as high as those of FRVB in parallel. Each sub-cell of FDEB was connected in different ways according to actual requirements. Different output currents and voltages were obtained, whereas no difference was observed in output power. Moreover, the energy deposition of X-ray at each AlGaInP or ZnS:Cu layer in FDEB was simulated by using MCNP5. A small amount of energy deposition in the fluorescent layer significantly improved the electrical output performance of the nuclear battery. A multilayer dual-effect energy conversion mechanism improved the electrical output performance of the nuclear batteries.

1. Introduction

Nuclear batteries, as a micro-power supply devices, have great development potential and application value owing to the rapid development of micro-electromechanical systems (MEMSs) [1]. Nuclear batteries generate electricity by utilizing radioactive particles or rays emitted by radioisotope decay or by utilizing heat released by radioisotope decay. Radio-voltaic battery (RVB) and radio-luminescence battery (RLB) are the two typical representatives of nuclear batteries and have been proven to have long service lives, strong adaptability, and high stability, and they do not require energy recharging during their service periods. Furthermore, they can be miniaturized [2–4].

Different energy conversion structures and materials have been used for the improvement of the electrical output performance levels of RVBs and RLBs [5–8]. However, their output power levels remain low and are often at the order of nW − μW [9–12]. MEMSs are potential application objects of nuclear battery and have a certain requirement for output power. Moreover, β radioisotopes, such as ^{147}Pm, ^{63}Ni, and ^{90}Sr, are frequently used as energy sources for RVBs and RLBs [13,14]. High-energy beta particles can easily cause irradiation damage on energy conversion materials and consequently impair battery performance. Thus, the radioactive sources of low-energy beta particles are often preferred as energy sources for nuclear batteries. However, these sources have a serious self-absorption effect [15], which causes low surface emission density. This effect hinders the increase in output power.

In contrast to β particles, X-ray or γ-ray have a strong penetration ability and low self-absorption effect and thus potential alternatives as energy sources for nuclear batteries. The energy of X-/γ-rays can be completely deposited in the energy conversion unit by designing an appropriate energy conversion structure and adopting suitable energy conversion materials for high electrical output. Moreover, they can effectively reduce irradiation damage in semiconductor materials and thus may prolong the service life of a nuclear battery [16]. Furthermore, high-activity gamma radiation sources, such as ^{137}Cs and ^{60}Co, can be easily obtained.

X-ray or γ-ray is sometimes used for nuclear battery research. Butera et al. fabricated a nuclear battery based on a ^{55}Fe X-ray radioisotope [17]. Lee et al. utilized spent fuel in nuclear power plants and proposed the use of RLB for the conversion of abundant γ decay energy in spent fuel to electricity [18]. In our previous work, we proposed the concept of a multilayer dual-effect nuclear battery based on the radio-voltaic

* Corresponding author.
E-mail address: tangxiaobin@nuaa.edu.cn (X. Tang).

https://doi.org/10.1016/j.nimb.2018.05.026
Received 21 February 2018; Received in revised form 12 May 2018; Accepted 14 May 2018

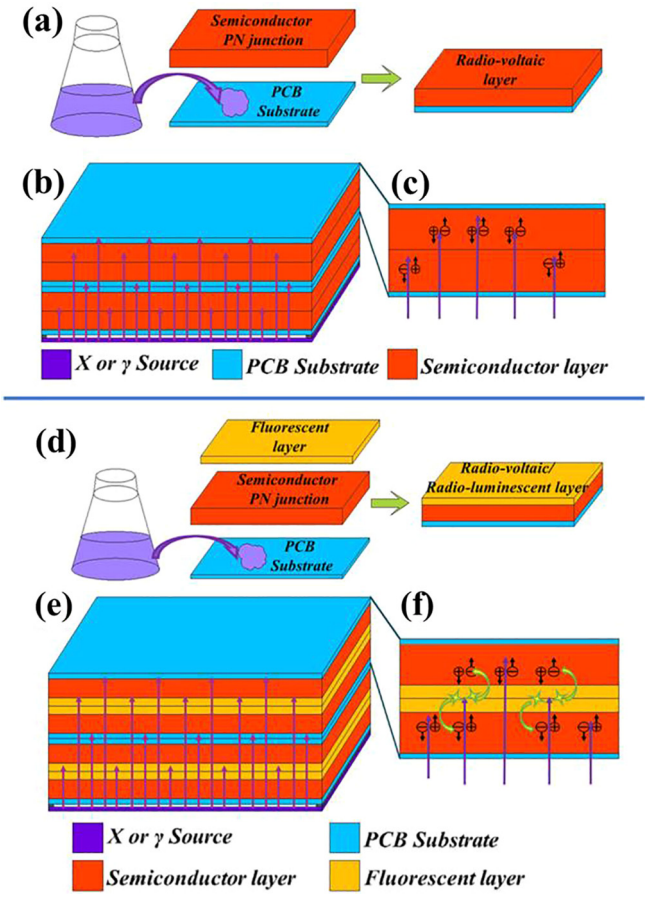

Fig. 1. (a) Sub-cell of FRVB with radio-voltaic layer; (b) FRVB; (c) working principle of FRVB; (d) sub-cell of FDEB with radio-voltaic/radio-luminescence layer; (e) FDEB; (f) working principle of FDEB.

effect and radio-luminescence effect [16]. We fabricated a new nuclear battery based on the X-ray tube, which utilizes scintillation crystals to enhance the performance of GaAs RVBs. However, this work employed a single-layer energy conversion structure.

In the present study, we prepared a four-layer dual-effect nuclear battery (FDEB) based on γ-ray, as shown in Fig. 1e. A four-layer radio-voltaic nuclear battery (FRVB) was also prepared for comparison, as shown in Fig. 1b. For FDEB, each sub-cell contains a radio-voltaic layer and a radio-luminescent layer. For FRVB, each sub-cell contains a radio-voltaic layer. The electrical performance of each sub-cell and those of batteries with different connection modes were tested under X-ray irradiation. The difference in performance between the two kinds of batteries was analyzed. The energy deposition of X-rays in the semiconductor and fluorescent materials of the batteries was simulated by using the Monte Carlo program MCNP5.

2. Materials and methods

2.1. Structural design and working principle

A low-atomic-number, low-density, and thin PCB plate was employed as substrate for the semiconductor PN junction (Fig. 1a). Those two parts were connected with silver paste. A radio-voltaic layer with a volume of 0.25 cm^3, which is considered a sub-cell of the FRVB, was prepared (Fig. 2). An FRVB consists of four radio-voltaic layers (Fig. 1b).

A radio-voltaic/radio-luminescence layer, which is frequently used as a sub-cell of the FDEB, is composed of a radio-voltaic layer and fluorescent layer. Four radio-voltaic/radio-luminescence layers were

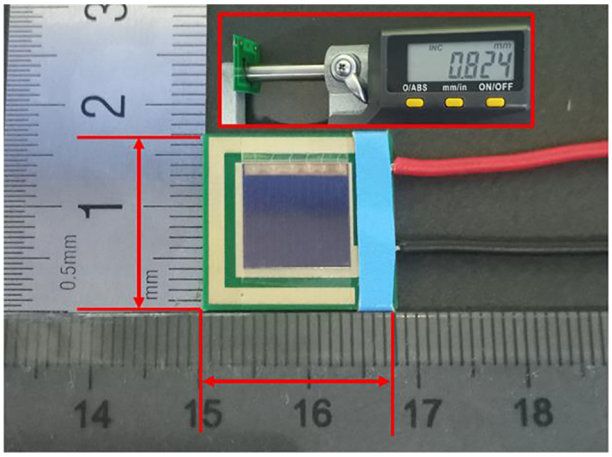

Fig. 2. Sample and size of radio-voltaic layer.

combined for the fabrication of an FDEB (Fig. 1e). For the FDEB, the fluorescent layers of every two sub-cell were adjacent to each other, that is, two fluorescent layers were clamped by two radio-voltaic layers. The isotropic radio-luminescent photons generated by the fluorescent layer were maximally collected by the radio-voltaic layer and converted into electric energy.

The working principle of the FRVB is shown in Fig. 1c. X-rays or γ-rays generate a large number of electron-hole pairs (EHPs) by ionization and excitation in semiconductor materials, which are separated by the action of a built-in electric field and form the radiation current.

The working principle of the FDEB is shown in Fig. 1f. The energy conversion process has two parts. In the first part, radiation energy is converted to electricity through the radio-voltaic effect. This conversion occurs in FDEB and FRVB. In the second part, radiation energy is converted first to photon energy and then to electricity through the radio-photovoltaic effect. X-rays or γ-rays generate isotropic fluorescence photons in the fluorescent layer by excitation. These fluorescent photons interact with the semiconductor PN junction to create EHPs that are drawn off as current through the photoelectric effect.

2.2. Materials

AlGaInP and ZnS:Cu were used as semiconductor and fluorescent materials, respectively. The radiation resistance rates of the nuclear batteries are directly related to the bandgap widths of the semiconductor materials. A wide bandgap semiconductor shows strong resistance to irradiation. Most previous studies on RVB and RLB employ Si or GaAs as the semiconductor PN junction due to their mature production technology [3,19]. However, Si and GaAs have a small band gap, which results in poor radiation resistance. The present study used AlGaInP as a semiconductor PN junction material with a band gap of 2.05 eV (The band gap of AlGaInP is determined by photoluminescence (PL) using a focused micro-Raman system (LabRAM-RH, J.Y.), under room temperature). AlGaInP should have better radiation resistance and consequently a longer service life than Si and GaAs [20]. The effective size of the AlGaInP semiconductor PN junction used in this study is 10 mm × 10 mm × 0.373 mm, which was placed on the PCB substrate of 0.4 mm thick using silver paste. The prototype and structure schematic of the AlGaInP semiconductor PN junction are illustrated in Fig. 3. A transparent film was covered on the surface to protect the front structure of the PN junction.

A ZnS:Cu fluorescent powder was deposited on the Biaxially Oriented Polypropylene (BOPP) substrate with high transmittance to form a ZnS:Cu fluorescent layer with a thickness of 70 ± 5 μm, as shown in Fig. 4a. Fig. 4b provides the transmittance curve of BOPP and the emission spectrum of ZnS:Cu. The transmittance of BOPP is 88.28% at the peak of the emission spectrum of ZnS:Cu, that is 530 nm. High

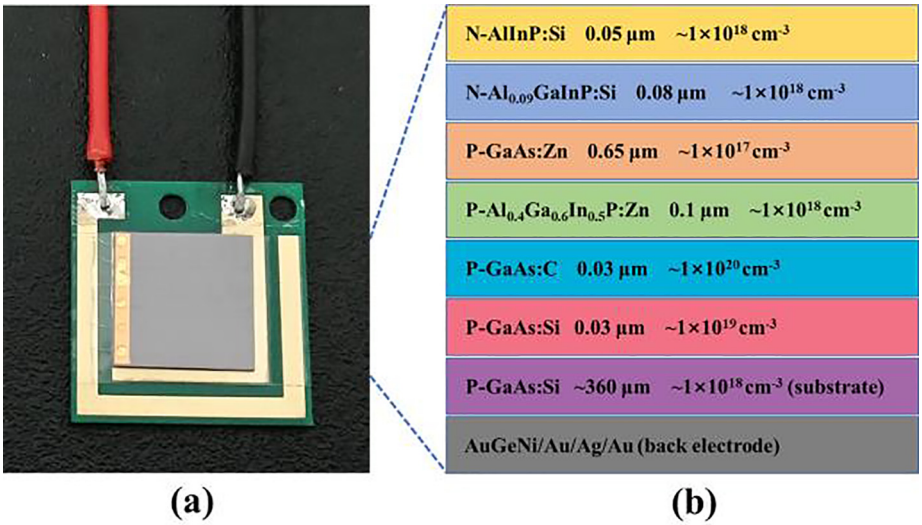

Fig. 3. (a) Prototype and (b) structure schematic of the AlGaInP semiconductor PN junction.

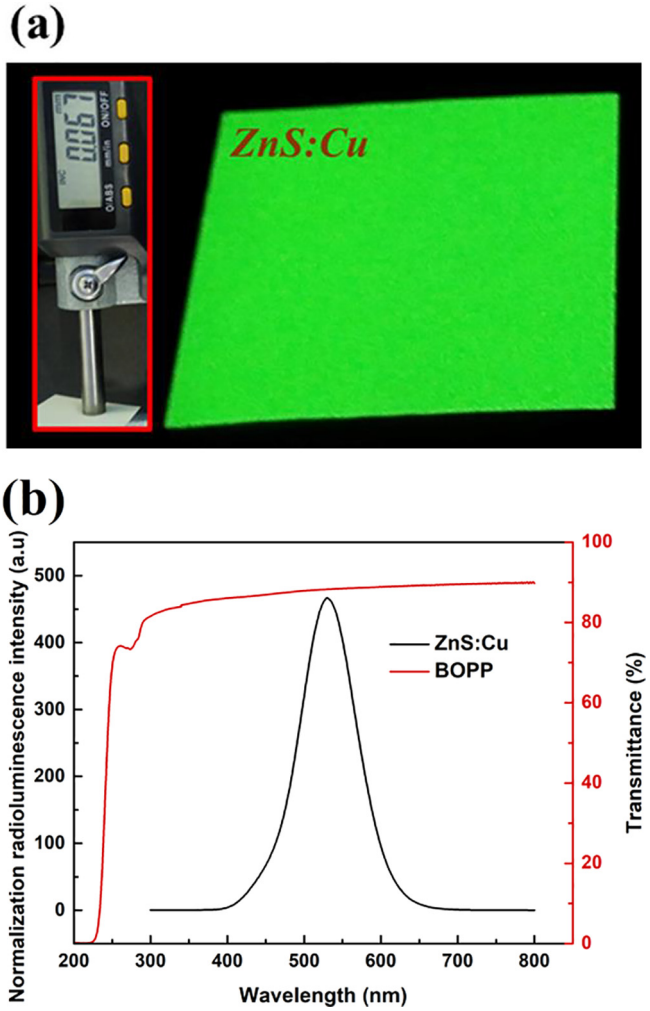

Fig. 4. (a) ZnS:Cu fluorescent layer; (b) BOPP transmittance and ZnS:Cu radio-luminescence spectrum.

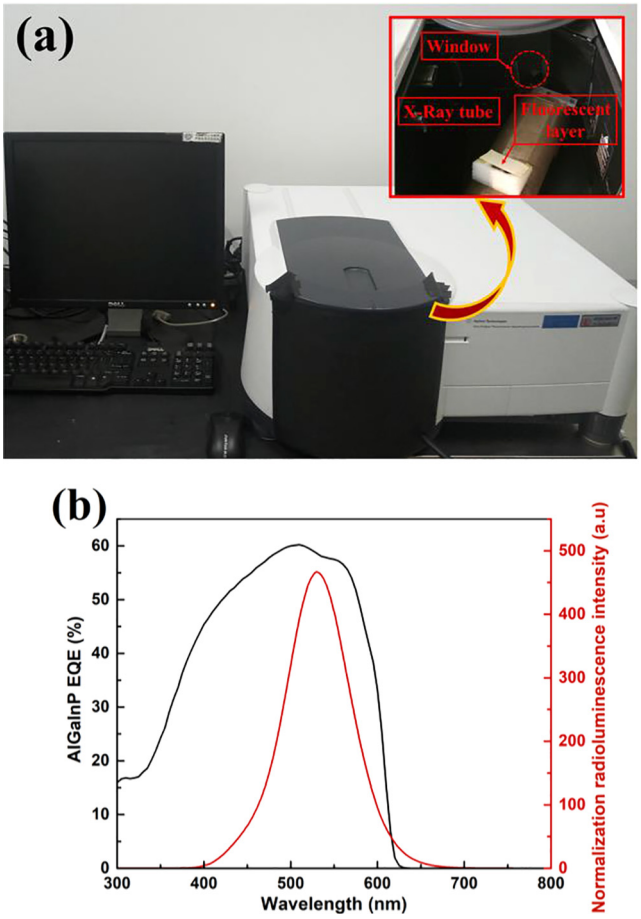

Fig. 5. (a) Test system of ZnS:Cu radio-luminescence spectrum; (b) Radio-luminescence spectrum of ZnS:Cu fluorescent layer and quantum response efficiencies of the AlGaInP semiconductor PN junction.

transparency can ensure that the radio-luminescence photons have less self-absorption and high emission rate.

The radio-luminescence spectrum of the ZnS:Cu fluorescent layer under X-ray irradiation was measured with a Cary Eclipse fluorescence spectrophotometer (Agilent Technologies G9800a, Malaysia; Fig. 5a). The quantum efficiencies of the AlGaInP radio-voltaic layers were tested by quantum efficiency test system (Bentham, PVE300) under room temperature. The radio-luminescence spectrum of the fluorescent materials and the quantum efficiency of the semiconductor PN junction are shown in Fig. 5b. AlGaInP has high quantum response efficiency at almost the whole range of the radio-luminescence spectrum. The peak

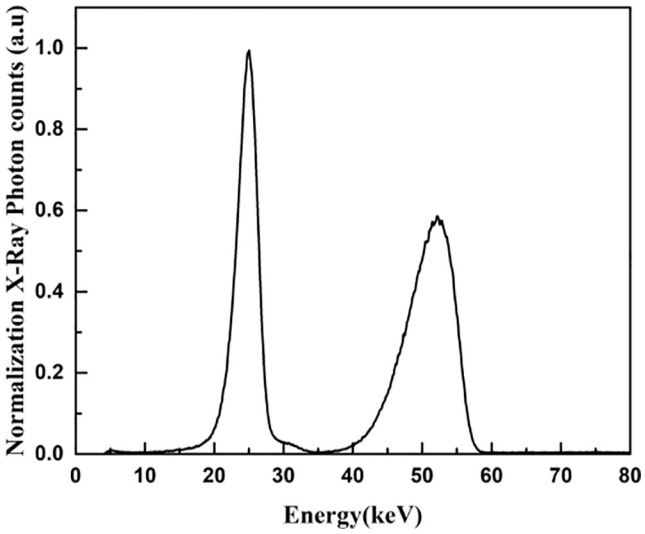

Fig. 6. X-ray energy spectrum of the X-ray tube.

of the fluorescent layers' radio-luminescence spectrum is 530 nm. For the AlGaInP radio-voltaic layers in this article, the quantum efficiency reaches 59.91% at 530 nm fluorescence wavelength. This result shows that the AlGaInP semiconductor PN junction matches the ZnS:Cu fluorescent layer well.

2.3. X-ray energy spectrum of X-ray tube

In this study, an X-ray tube (Shanghai KeyWay Electron Company Ltd. KYW900A, China) was used to instead of gamma source to test the output performance of nuclear batteries. The voltage and current of the X ray tube were set to 60 kV and 900 μA, respectively. The X-ray energy spectrum was measured with the radiation detector system (CzT probe, Shanxi detek; Multichannel pulse amplitude analyzer, model: ORTEC 946; Preamplifier, MODEL: ORTEC 572A), as shown in Fig. 6. The average X-ray energy of the X-ray tube is 39.31 keV.

3. Test and discussion

3.1. Electrical output performance of FRVB

Fig. 7a shows the structure diagram of FRVB. Fig. 7b shows the 17 mm × 18 mm × 3.26 mm sample. The electrical performance of each sub-cell and those of the batteries with different connection modes were tested under X-ray irradiation. The sub-cells of FRVB were numbered 1#, 2#, 3#, and 4# by their respective positions to the X-ray tube (Fig. 8).

The *I-V* and *P-V* curves of each sub-cell and the whole batteries with different connection modes are shown in Fig. 9a and b, respectively. The open circuit voltage (V_{oc}), short circuit current (I_{sc}), fill factor (*FF*), and maximum output power (P_{max}) were extracted from *I-V* and *P-V* curves and shown in Table 1. The terms of R1 and R2 refer to the FRVB in series and parallel, respectively. P_{max} and *FF* can be expressed as follows:

$$P_{max} = V_{max} \times I_{max} \text{ and} \tag{1}$$

$$FF = \frac{P_{max}}{V_{oc} \times I_{sc}} = \frac{V_{max} \times I_{max}}{V_{oc} \times I_{sc}} \times 100\% \tag{2}$$

The energy of X-rays and the energy deposited in the energy conversion materials varies with the increase of penetration depth, which results in the different output performance of each sub-cell. The X-ray energy spectrum obtained in this study was used as the initial source condition. The energy of X-ray deposited in each sub-cell of the FRVB was simulated by the Monte Carlo program MCNP5_RSICC_ 1.14 (Los Alamos National Laboratory (LANL)). Fig. 10 is the FRVB geometry model built by the MCNP5 program. In order to get the simulation results of small errors, we set up 3×10^7 photons to bombardment FRVB. The simulation results show that the error is less than 0.004 in the area of investigation. Fig. 11 shows that the energy deposition in the energy conversion materials gradually decreases as the penetration depth increases. High deposited energy produces high I_{sc} and high P_{max}.

As predicted, the I_{sc} and P_{max} of sub-cells 1# and 2# are larger than those of sub-cells 3# and 4#, respectively, and the smallest one is 4#. According to the theoretical results of energy deposition, the I_{sc} and P_{max} of sub-cell 1# should be slightly larger than those of sub-cell 2#, respectively. However, the measured results present the opposite case. This phenomenon may be due to the difference in the characteristics of the semiconductor PN junction, which includes dark current and reverse saturation current. The relationship between applied voltage (V) and dark current (I_d) in the radio-voltaic layer can be expressed as:

$$\ln(I_d) = \frac{q}{nKT}V + \ln(I_0) \tag{3}$$

where *n* is the ideal factor, *q* is the electron charge, *K* is the Boltzmann constant, I_0 is the saturation current, I_d is the dark current, and *V* is the applied voltage.

The dark characteristics of the four radio-voltaic layers were swept from −1 V to 1 V, as shown in Fig. 12. The forward current at 1 V is about 8.82×10^3 times larger than the reverse one at −1 V for 1# radio-voltaic layer, 1.26×10^5 times for 2#, 2.00×10^5 times for 3#, 6.07×10^3 times for 4#. That shows the four radio-voltaic layers have good rectifying characteristics. However, their rectifying characteristics vary greatly. This may be due to the limitations of the processing technology.

Linear fittings were performed on the forward current-voltage curves using equation 3 at room temperature (Fig. 12(a') (b') (c') (d')), the ideality factors and saturation currents of the four radio-voltaic layers were, respectively, the slopes and the intercepts obtained in the linear fittings. The saturation current of 4# radio-voltaic layer is the largest and about 155 times larger than 2#. Combining saturation current and rectifying characteristic, we can conclude that 2# radio-voltaic layer has the best quality.

Fig. 9a and Table 1 show that the values of I_{sc} for the four sub-cells vary greatly. The largest value is 17.35 nA for 2#, which is more than 12 times larger than the smallest value of 1.36 nA for 4#. There are two

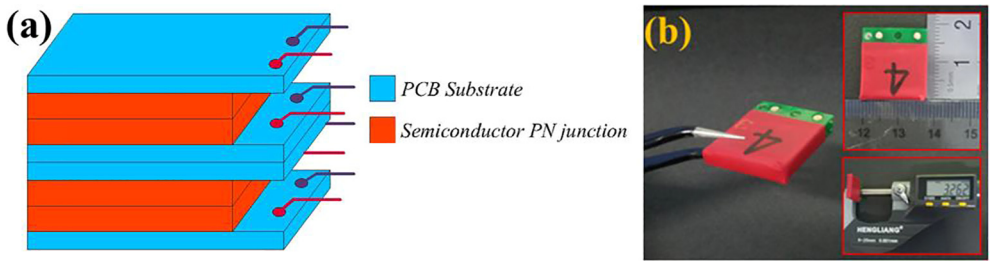

Fig. 7. (a) Structure diagram of FRVB; (b) sample and size of FRVB.

Fig. 8. Electrical output performance test system for nuclear battery.

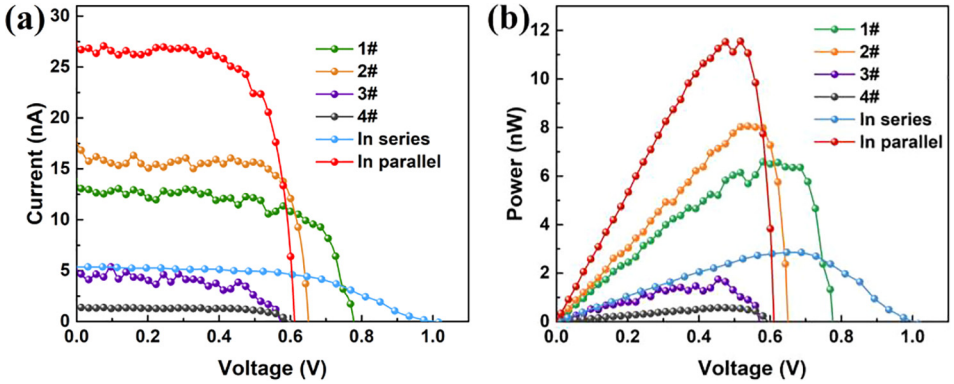

Fig. 9. (a) *I-V* curves of FRVB; (b) *P-V* curves of FRVB.

Table 1
Output performance of FRVB.

Electrical performances	Sub-cells of FRVB				FRVB with different connection modes	
	1#	2#	3#	4#	Series (R1)	Parallel (R2)
I_{sc} (nA)	13.48	17.35	5.07	1.36	5.36	27.04
V_{oc} (V)	0.78	0.65	0.59	0.59	1.00	0.61
P_{max} (nW)	6.58	8.06	1.83	0.57	2.86	11.55
FF (%)	62.58	71.47	61.18	71.04	53.36	70.02

reasons for this. On the one hand, the energy deposition produced by X-rays in the two sub-cells is different; on the other hand, the quality of the 4# sub-cell is worse than that of the 2# sub-cell. The differences between the values of V_{oc} for the four sub-cells are not big. The largest V_{oc} of 0.78 V for 1# is only 1.3 times higher than the smallest V_{oc} of 0.59 V for 4#.

Table 1 shows that the I_{sc} of FRVB in series is 5.36nA, which is far less than 1# and 2# sub-cell's I_{sc}. The V_{oc} of FRVB in series (1.00 V) is less than the sum of the V_{oc} of the four sub-cells (2.61 V). The four sub-

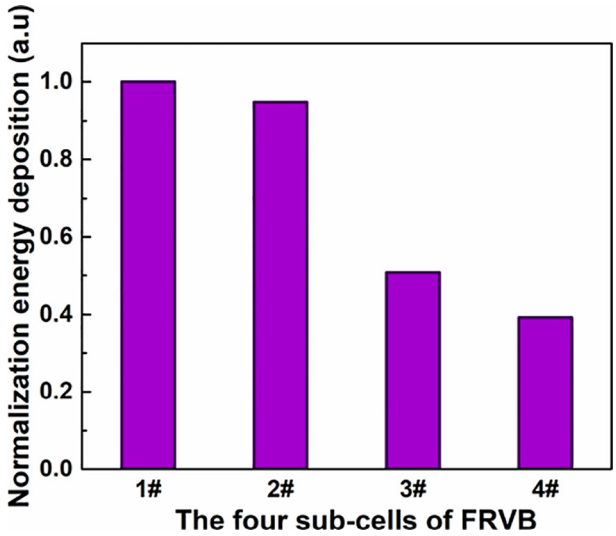

Fig. 11. Energy deposition of X-ray generated in each sub-cell of FRVB.

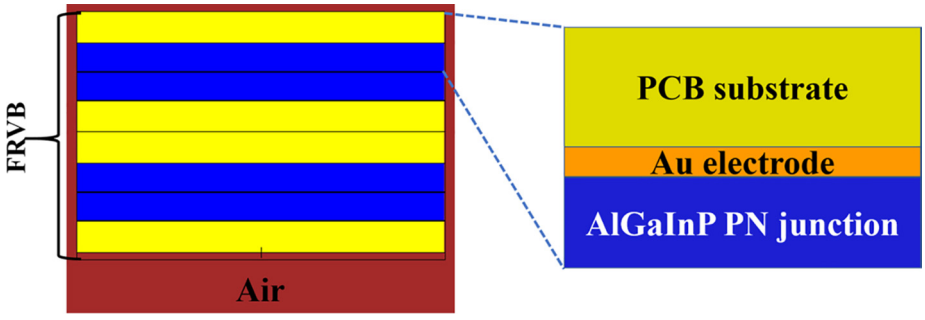

Fig. 10. Geometry model of FRVB built by the MCNP5 program.

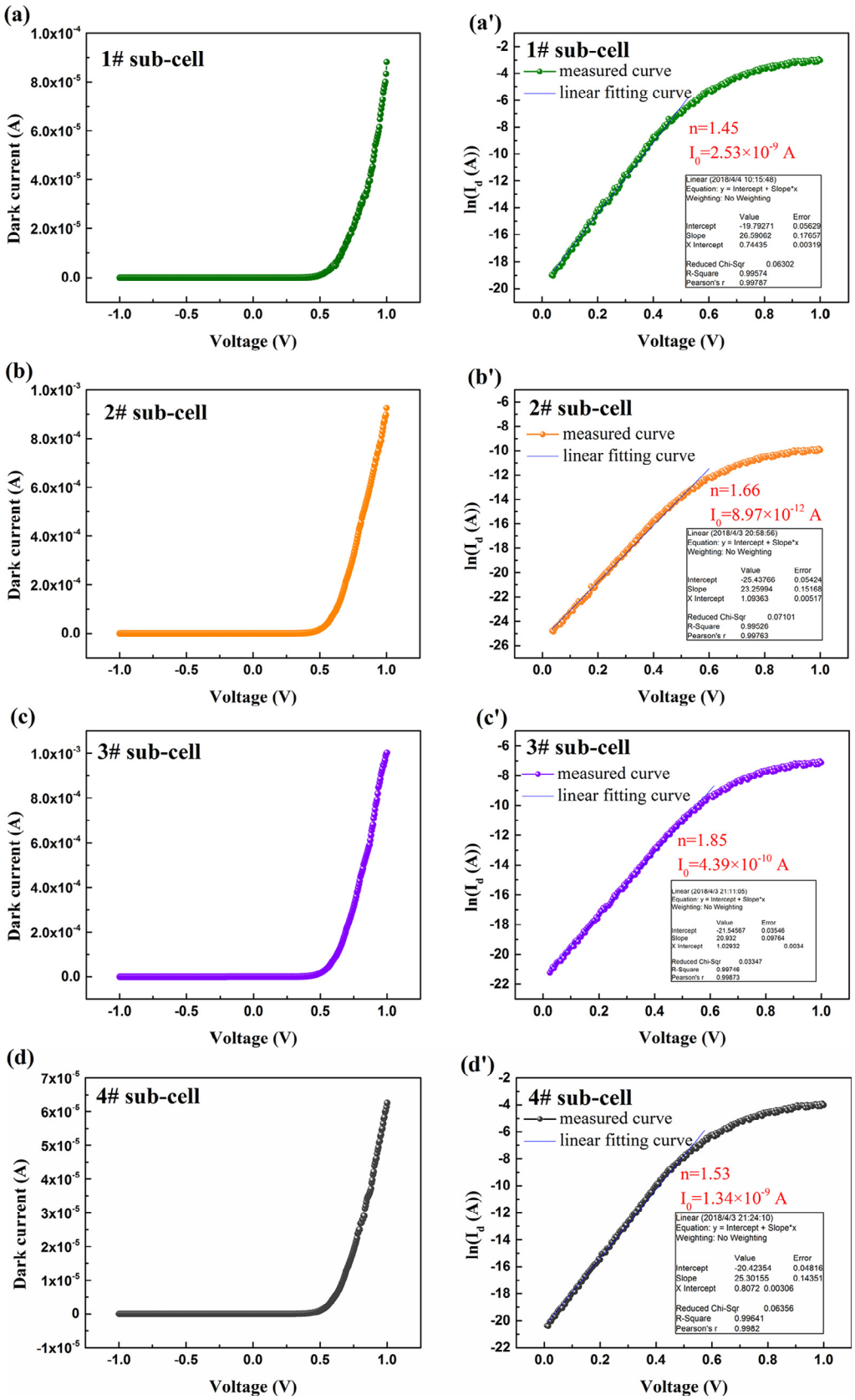

Fig. 12. The dark characteristics of (a) 1#, (b) 2#, (c) 3#, (d) 4# radio-voltaic layer. (a′), (b′), (c′), (d′) shows the I-V curves (ln scale) at forward direction, and the linear fitting curve of the forward *I–V* characteristics.

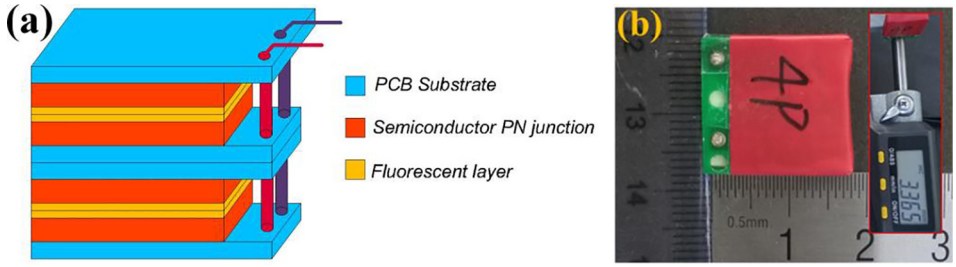

Fig. 13. (a) Structure diagram of FDEB; (b) the sample and size of FDEB.

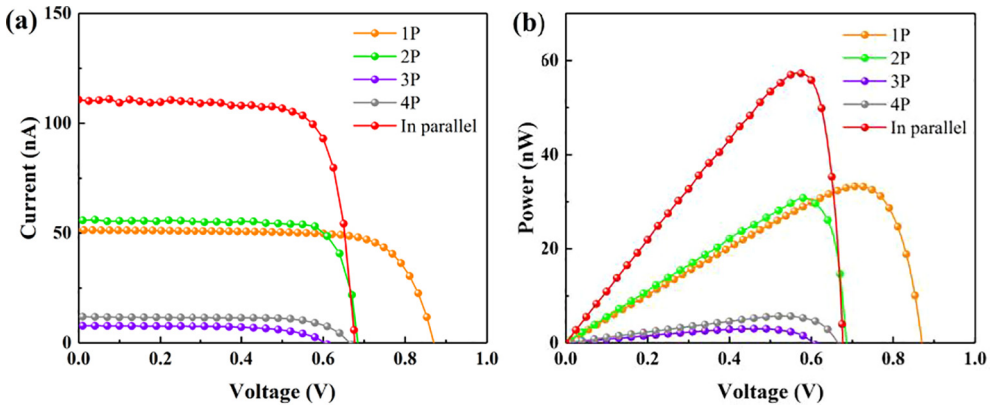

Fig. 14. (a) *I-V* curves of FDEB; (b) *P-V* curves of FDEB.

Table 2
The electrical output performance of dual-effect nuclear batteries.

Electrical performances	Sub-cells of FDEB				FDEB in parallel (D1)
	1P	2P	3P	4P	
I_{sc} (nA)	51.40	55.96	7.75	11.31	110.45
V_{oc} (V)	0.86	0.69	0.60	0.69	0.69
P_{max} (nW)	33.27	30.81	2.83	6.03	57.26
FF (%)	75.26	79.79	60.86	77.27	75.13

cells in the series circuit have different electrical output, especially their current varies greatly. Due to the mismatch of the currents of the four sub-cells, unnecessary voltage loss occurs in the series circuit. The P_{max} of FRVB in series is almost six times smaller than the sum of the P_{max} of the four sub-cells. No big difference is observed between the I_{sc} and P_{max} of FRVB in parallel and the sums of I_{sc} and P_{max} of the four sub-cells. The V_{oc} of FRVB in parallel is close to the average V_{oc} of the four sub-cells.

The parallel mode significantly achieves better electrical output performance compared with the series mode. The short circuit current of each battery needs to be matched when multiple batteries are connected in series. The I_{sc} of each sub-cell of FRVB has a big difference due to the penetration law of the X-ray. When a series circuit is formed, the small I_{sc} of the sub-cell becomes the load of the large one, which leads to large amounts of energy loss and poor electrical output performance. The matching of the V_{oc} of each battery is important when several batteries are connected in parallel. The measured results show that the V_{oc} of the four sub-cells is close to each other. The V_{oc} of FRVB in parallel does not drop significantly. Large I_{sc} and P_{max} are obtained. This result reveals that a parallel circuit is a good option for the four-layer nuclear battery proposed in this study.

3.2. Electrical output performance of FDEB

Fig. 13a shows the structure diagram of FDEB. Fig. 13b gives the sample with the size of 17 mm × 18 mm × 3.37 mm, which is approximately 1.03 cm^3. The electrical performances of each sub-cell and the whole batteries with different connection modes were tested under X-ray irradiation, respectively. The sub-cells of FDEB were numbered 1P, 2P, 3P, and 4P by their respective positions to the X-ray tube.

The *I-V* and *P-V* curves of each sub-cell and FDEB in the parallel mode are shown in Fig. 14a and 14b. The V_{oc}, I_{sc}, *FF*, and P_{max} were extracted from *I-V* and *P-V* curves and shown in Table 2. The term of D1 refers to the FDEB in parallel.

The results in Tables 2 and 1 show that FDEB significantly achieves a better electrical output performance than FRVB after introducing four thin fluorescent layers. For example, the P_{max} of FDEB in parallel (57.26 nW) is approximately five times larger than that of FRVB, and the I_{sc} of FDEB increases 5 times FRVB. The volume of FDEB only increases by 0.03 cm^3 with respect to 1 cm^3 of FRVB. Moreover, the I_{sc} and P_{max} of sub-cells 1P and 2P are larger than those of sub-cells 3P and 4P, respectively. Compared with 3P and 4P, 1P and 2P are closer to the X-ray source, the I_{sc} of 1P and 2P are both significantly greater than 3P

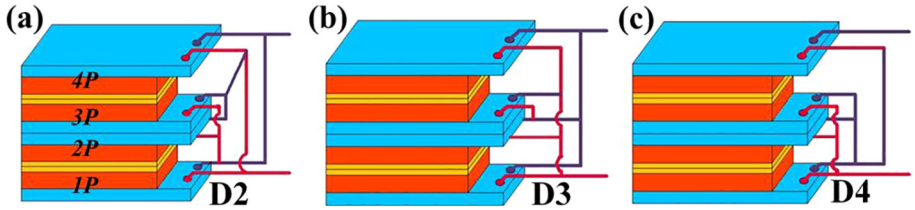

Fig. 15. FDEB with different connection modes.

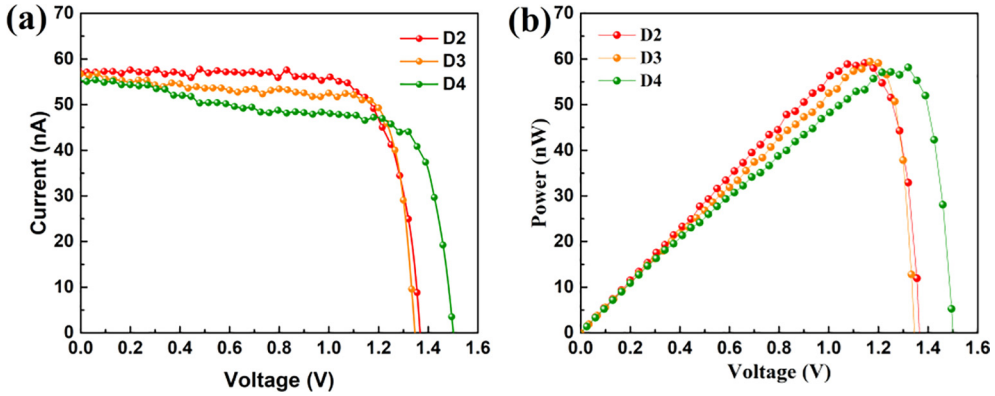

Fig. 16. (a) *I-V* curves of FDEB different connection modes; (b) *P-V* curves of FDEB with different connection modes.

Table 3
Electrical output performance of FRVB with different connection modes.

Electrical performances	FRVB with different connection modes		
	D2	D3	D4
I_{sc} (nA)	57.39	56.54	55.26
V_{oc} (V)	1.37	1.35	1.51
P_{max} (nW)	59.11	59.40	58.15
FF (%)	75.18	77.82	69.69

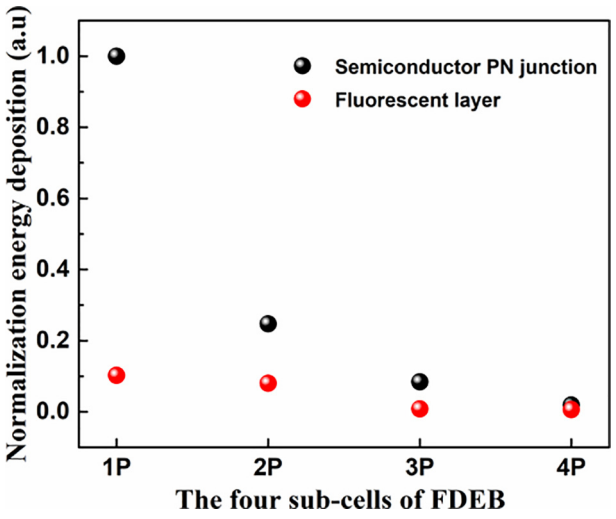

Fig. 17. Ratio of energy deposited by each semiconductor PN junction and each fluorescent layer in FDEB.

and 4P. However, the I_{sc} of 2P is slightly greater than 1P, and 4P is slightly larger than 3P. We consider there are several reasons for those. Firstly, 1P and 2P are in close proximity, so are 3P and 4P. The intensities of the radio-fluorescence captured by 1P and 2P or 3P and 4P are almost the same. Secondly, the quality and performance of the semiconductor layers are not exactly same like each other. Last but not least, the thickness of the fluorescent layer has an error of ± 5 μm, which perhaps contributes to the results. The specific reasons for this issue require further study. The values of V_{oc} have minimal differences, which is similar to FRVB.

3.2.1. FDEB with different connection modes

Different electron devices have different requirements on the electrical output properties of the nuclear battery. FDEB can output different voltage and current by changing the connection between the sub-cells to meet the demand of electric appliances. Fig. 15 shows that three

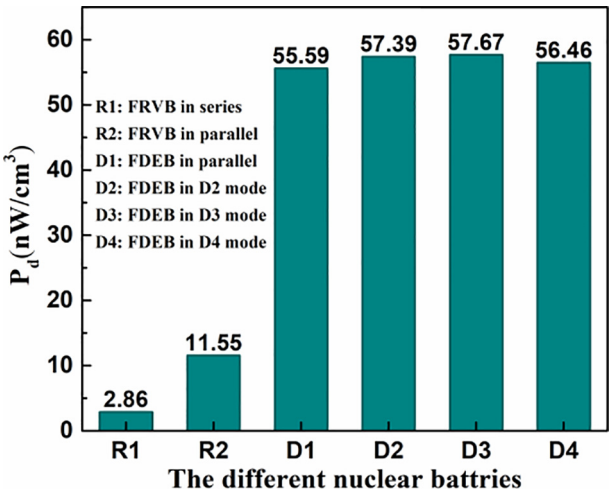

Fig. 18. Output power density of different nuclear battery.

other connections were carried out on FDEB except for FDEB in parallel. For the first connection, sub-cells 1P and 4P were connected in parallel and so were 2P and 3P. The two parts were connected in series. We called this connection D2, as shown in Fig. 15a. For the second connection, 1P, 3P, and 4P were connected in a parallel. This part was connected with 2P in series to obtain D3, as shown in Fig. 15b. For the third connection, 2P, 3P, and 4P were connected in parallel. This part was connected with 1P in series to obtain D4, as shown in Fig. 15c. The electrical performances of D2, D3, and D4 were tested under the irradiation of the X-ray tube with 60 kV and 900 μA. The *I-V* and *P-V* curves are shown in Fig. 16a and b, respectively. V_{oc}, I_{sc}, *FF*, and P_{max} were extracted from *I-V* and *P-V* curves and shown in Table 3.

Compared with the FDEB in parallel, D2, D3, and D4's I_{sc} decreases by approximately 50%, their V_{oc} increases approximately by 100%, and their P_{max} is almost unchanged. The test results show that the current and voltage of FDEB can be changed by different connection modes without the loss of power to meet the needs of electron devices.

3.2.2. Energy deposition

The energy deposition generated by X-rays in each semiconductor PN junction and fluorescent layers of the FDEB was simulated by MCNP5. Fig. 17 shows that the energy deposition in the semiconductor PN junction and the fluorescent material gradually decreases with the increase of X-ray penetration depth. The energy deposition in the semiconductor PN junction is higher than the energy deposition in the fluorescent layer. In the entire FDEB, the energy deposited in the semiconductor PN junction layers is approximately 4.95 times in fluorescent layers. The fluorescent layer can significantly enhance the electrical output performance by comparing FDEB and FRVB although

the energy deposited in the fluorescent layer is much lower than that in the PN junction layer. This phenomenon proves that it effectively improves the electrical output performance of the nuclear battery by using a dual-effect energy conversion mechanism with a multilayer structure.

3.3. Output power density

In addition to I_{sc}, V_{oc}, P_{max}, and FF, power density (P_d) is also an important performance parameter for the nuclear battery and can be expressed as follows:

$$P_d = \frac{P_{out}}{V_b} \tag{4}$$

where the unit of P_d is nW/cm^2, P_{out} is the output power that is equal to P_{max}, and V_b is the volume of the whole battery.

Fig. 18 shows that the P_d of FDEB is much larger than that of FRVB. The largest P_d for FDEB is 57.67 nW/cm^3 of the connection way D3. The largest P_d for FRVB is 11.55 nW/cm^3 of the parallel mode.

4. Conclusion

We prepared four-layer radio-voltaic and dual-effect nuclear batteries based on X-ray, AlGaInP semiconductor PN junction, and ZnS:Cu fluorescent materials. The volume of the former was 1.00 cm^3, and that of the latter was 1.03 cm^3. The output performance levels of the two batteries were tested with the irradiation of the X-ray tube. The results showed that the output power of the nuclear battery in parallel was significantly greater than that in the series. The electrical output performance of FDEB was significantly better than that of FRVB. The P_{max} and P_d of FDEB in parallel were 57.26 nW and 55.59 nW/cm^3, respectively, which were both five times as high as those of FRVB in parallel. Thus, the feasibility and superiority of using the dual-effect energy conversion mechanism improved the electrical output performance levels of the nuclear batteries. To meet the demands of different electric appliances, we obtained different currents and voltages by changing the connection mode of each sub-cell of FDEB without the loss of the output power.

Moreover, the X-ray energy deposited in the semiconductor PN junction and the fluorescent layers of FDEB were simulated by Monte Carlo program MCNP5. The energy deposited in the fluorescent layer is far lower than that in the semiconductor PN junction. By comparing the electrical output performance of FDEB with that of FRVB, we found that a small amount of energy deposition in the fluorescent layer can significantly improve the electrical output performance of a nuclear battery. This phenomenon proves that the electrical output performance levels of nuclear batteries can be improved by using the layer through a multilayer dual-effect energy conversion mechanism.

Acknowledgments

This work was supported by the National Natural Science Foundation of China (Grant Nos. 11675076 and 11505096), the Natural Science Foundation of Jiangsu Province (Grant No. BK20150735), the Shanghai Aerospace Science and Technology Innovation Project (Grant No. SAST2016112) and the Foundation of Graduate Innovation Center in NUAA (Grant No. kfjj20170603).

References

[1] Z.H. Xu, X. Bin Tang, L. Hong, Y.P. Liu, D. Chen, Structural effects of ZnS: Cu phosphor layers on beta radioluminescence nuclear battery, J. Radioanal. Nucl. Chem. 303 (2015) 2313–2320, http://dx.doi.org/10.1007/s10967-014-3655-3.
[2] J. Russo, M. Litz, W. Ray, G.M. Rosen, D.I. Bigio, R. Fazio, Development of tritiated nitroxide for nuclear battery, Appl. Radiat. Isot. 125 (2017) 66–73, http://dx.doi.org/10.1016/j.apradiso.2017.04.013.
[3] F. Rahmani, H. Khosravinia, Optimization of Silicon parameters as a betavoltaic battery: comparison of Si p-n and Ni/Si Schottky barrier, Radiat. Phys. Chem. 125 (2016) 205–212, http://dx.doi.org/10.1016/j.radphyschem.2016.04.012.
[4] D.S. Cheu, T.E. Adams, S.T. Revankar, Experiments and modeling on effects of temperature on electrical performance of a betavoltaic, Nucl. Eng. Des. 325 (2017) 256–260, http://dx.doi.org/10.1016/j.nucengdes.2017.06.028.
[5] C.C. Chen, Y.Y. Chang, J.W. Zhang, A novel betavoltaic microbattery based on SWNTs thin film-silicon heterojunction, Proceedings of the IEEE International Conference on Micro Electro Mechanical Systems (MEMS), 2012, pp. 1197–1200, , http://dx.doi.org/10.1109/MEMSYS.2012.6170378.
[6] H. Guo, A. Lal, Nanopower betavoltaic microbatteries, Digest of Technical Papers, TRANSDUCERS 2003 – 12th International Conference on Solid-State Sensors, Actuators and Microsystems, 2003, pp. 36–39, , http://dx.doi.org/10.1109/SENSOR.2003.1215247.
[7] H. San, S. Yao, X. Wang, Z. Cheng, X. Chen, Design and simulation of GaN based Schottky betavoltaic nuclear micro-battery, Appl. Radiat. Isot. 80 (2013) 17–22, http://dx.doi.org/10.1016/j.apradiso.2013.05.010.
[8] S. Theirrattanakul, M. Prelas, A methodology for efficiency optimization of betavoltaic cell design using an isotropic planar source having an energy dependent beta particle distribution, Appl. Radiat. Isot. 127 (2017) 41–46, http://dx.doi.org/10.1016/j.apradiso.2017.05.005.
[9] Q. Zhang, N. Wang, P. Zhou, C. Chen, H. San, K. Wang, X. Chen, A betavoltaic microbattery using zinc oxide nanowires under build in potential difference, Proceedings of the IEEE International Conference on Micro Electro Mechanical Systems (MEMS), 2016, pp. 1177–1180, , http://dx.doi.org/10.1109/MEMSYS.2016.7421846.
[10] C. Thomas, S. Portnoff, M.G. Spencer, High efficiency 4H-SiC betavoltaic power sources using tritium radioisotopes, Appl. Phys. Lett. 108 (2016), http://dx.doi.org/10.1063/1.4939203.
[11] S. Butera, G. Lioliou, A.B. Krysa, A.M. Barnett, Temperature dependence of an AlInP ^{63} Ni betavoltaic cell, J. Appl. Phys. 120 (2016) 144501, http://dx.doi.org/10.1063/1.4964504.
[12] N. Ayarcı Kuruoğlu, O. Özdemir, K. Bozkurt, Betavoltaic study of a GaN p-i-n structure grown by metal-organic vapour phase epitaxy with a Ni-63 source, Thin Solid Films 636 (2017) 746–750, http://dx.doi.org/10.1016/j.tsf.2017.07.033.
[13] O. Artun, A study of nuclear structure for ^{244}Cm, ^{241}Am, ^{238}Pu, ^{210}Po, ^{147}Pm, ^{137}Cs, ^{90}Sr and ^{63}Ni nuclei used in nuclear battery, Mod. Phys. Lett. A 32 (2017) 5–8, http://dx.doi.org/10.1142/S0217732317501176.
[14] S. Rahastama, A. Waris, Analytical study of 90Sr betavoltaic nuclear battery performance based on p-n junction silicon, J. Phys. Conf. Ser. (2016), http://dx.doi.org/10.1088/1742-6596/739/1/012003.
[15] Y. Peng Liu, X. Bin Tang, Z. Heng Xu, L. Hong, H. Wang, M. Liu, D. Chen, Influences of planar source thickness on betavoltaics with different semiconductors, J. Radioanal. Nucl. Chem. 304 (2015) 517–525, http://dx.doi.org/10.1007/s10967-014-3879-2.
[16] Z.R. Zhang, X. Bin Tang, Y.P. Liu, Z.H. Xu, Z.C. Yuan, K. Liu, W. Chen, GaAs radiovoltaic cell enhanced by Y2SiO5crystal for the development of new gamma microbatteries, Nucl. Instrum. Meth. Phys. Res. B 398 (2017) 35–41, http://dx.doi.org/10.1016/j.nimb.2017.03.060.
[17] S. Butera, M.D.C. Whitaker, G. Lioliou, A.M. Barnett, AlGaAs 55 Fe X-ray radioisotope microbattery, Sci. Rep. 6 (2016), http://dx.doi.org/10.1038/srep38409.
[18] H. Lee, M.S. Yim, Examination of scintillator-photovoltaic cell-based spent fuel radiation energy conversion for electricity generation, Progr. Nucl. Energy 94 (2017) 46–54, http://dx.doi.org/10.1016/j.pnucene.2016.10.004.
[19] S. Butera, G. Lioliou, A.M. Barnett, Temperature effects on gallium arsenide 63Ni betavoltaic cell, Appl. Radiat. Isot. 125 (2017) 42–47, http://dx.doi.org/10.1016/J.APRADISO.2017.04.002.
[20] A.M. Ivanov, N.B. Strokan, A.A. Lebedev, Radiation hardness of a wide-bandgap material by the example of SiC nuclear radiation detectors, Nucl. Instrum. Meth. Phys. Res. Sect. A 675 (2012) 20–23, http://dx.doi.org/10.1016/j.nima.2012.01.047.